Research Square

Preprints are preliminary reports that have not undergone peer review.
They should not be considered conclusive, used to inform clinical practice,
or referenced by the media as validated information.

Operando X-ray scattering and pH tracking reveal a four stage crystallization pathway during calcium carbonate precipitation

Alain Gibaud

alain.gibaud@univ-lemans.fr

IMMM, UMR 6283 CNRS, Le Mans Université

özgür Gülmez

Department of Metallurgical and Materials Engineering, Middle East Technical University, 06800 Ankara, Turkiye https://orcid.org/0009-0006-9117-041X

Sandy Auguste

IMMM, UMR 6283 CNRS, Le Mans Université https://orcid.org/0000-0002-3777-9527

Basab Chattopadhyay

Department of Physics, Norwegian University of Science and Technology

Rodrigo Sanches Pires

ESRF

Seniz Ucar

Department of Metallurgical and Materials Engineering, Middle East Technical University

Yuriy Chushkin

ESRF

Article

Keywords:

Posted Date: August 4th, 2026

DOI: https://doi.org/10.21203/rs.3.rs-10221042/v1

License: This work is licensed under a Creative Commons Attribution 4.0 International License.
Read Full License

Additional Declarations: There is **NO** Competing Interest.

Operando X-ray scattering and pH tracking reveal a four stage crystallization pathway during calcium carbonate precipitation

Alain Gibaud,[1,2*] Özgür Gülmez,[3] Sandy Auguste,[1] Basab Chattopadhay,[4] Rodrigo Sanches Pires,[5] Seniz Ucar[3,6] and Yuriy Chushkin,[5*]

[1] *IMMM, UMR 6283 CNRS, Le Mans Université, 72085 Le Mans, France*

[2] *SWUST, Sichuan, Mianyang, Fucheng District, 青龙大道中段59号, 邮政编码: 621010, China*

[3] *Department of Metallurgical and Materials Engineering, Middle East Technical University, 06800 Ankara, Turkiye*

[4] *Department of Physics, Norwegian University of Science and Technology, Høgskoleringen 5, Trondheim 7491, Norway*

[5] *ESRF - The European synchrotron, 71 avenue des Martyrs, , 38000 Grenoble, France*

[6] *Department of Chemical Engineering, Norwegian University of Science and Technology, Høgskoleringen 5, Trondheim 7491, Norway*

(Dated: July 1, 2026)

Mineral formation proceeds through ultrafast structural transformations that are difficult to resolve experimentally, leaving the earliest stages of crystallization poorly understood. Here, operando synchrotron SAXS/WAXS combined with simultaneous pH monitoring resolves the real-time structural and chemical evolution of calcium carbonate precipitation under rapidly evolving, non-equilibrium supersaturation conditions. Four distinct stages are resolved: quasi-instantaneous formation of amorphous calcium carbonate (ACC) nanoparticles, the development of long-range density correlations preceding crystallization, the emergence of calcite and vaterite while ACC persists, and the progressive loss of amorphous coherence as calcite growth proceeds and vaterite disappears. The non-monotonic evolution of the Porod invariant, together with concomitant pH changes, provides model-independent markers of these stages, directly linking structural evolution to solution chemistry. These observations reveal a four-stage crystallization pathway and support a dissolution–reprecipitation mechanism involving a transient amorphous intermediate.

I. INTRODUCTION

The formation of crystalline solids from solution underpins processes ranging from geological mineralization to biomineralization and industrial scaling [1]. Yet, the kinetics of mineral precipitation by which dissolved species assemble into ordered structures—remains difficult to rationalize, as it reflects a complex interplay between solution chemistry and structural evolution across multiple length scales [2–6]. Calcium carbonate ($CaCO_3$) is a paradigmatic model system in this context, spanning environments from the slow growth of stalactites to biomineralization and rapid laboratory precipitation [7–10]. Across these settings, the sequence of phase transformations is highly sensitive to chemical and physical conditions, precluding a general predictive framework [11, 12].

A central challenge arises from the rapid onset of precipitation upon mixing precursor solutions, which can occur on sub-second timescales even at moderate supersaturation. Upon mixing Ca^{2+} and CO_3^{2-} solutions, the ionic activity product rapidly exceeds solubility limits, generating a highly supersaturated state typically associated with burst nucleation. However, this description is incomplete: supersaturation is not a static control parameter but evolves dynamically during the reaction as carbonate is consumed and solution chemistry changes. Because carbonate speciation is strongly controlled by pH, the effective supersaturation is continuously modulated by its value, introducing a feedback loop between precipitation and solution chemistry that is often neglected. In many experimental approaches, this coupling is further disrupted by constant-pH or buffered conditions [4, 13], which suppress natural chemical evolution and may alter reaction pathways.

Natural aqueous systems such as seawater highlight the importance of this feedback, remaining supersaturated with respect to $CaCO_3$ without spontaneous precipitation, reflecting kinetic inhibition and strong dependence on pH, ionic composition, and additives [13–

16]. These factors govern carbonate speciation and interfacial interactions, thereby controlling nucleation and growth pathways.

Interpretation is further complicated by the dependence of observed mechanisms on the experimental probe. Cryo-TEM, microfluidics, stopped-flow methods, and spectroscopic approaches access different temporal and spatial windows and often probe distinct regions of the kinetic landscape [3, 17–23]. Rather than providing a unified view, these methods can yield different mechanistic interpretations depending on whether the system is observed under quenched, flowing, or chemically constrained conditions.

These limitations highlight a key requirement: a quantitative, time-resolved description of precipitation must simultaneously capture both structural evolution and the evolving chemical state of the solution under unperturbed feedback conditions. To date, these aspects have largely been addressed separately. While synchrotron SAXS/WAXS provides access to particle formation and crystallization with millisecond resolution [13, 19, 24], such measurements are typically interpreted through model-dependent analyses and are rarely combined with direct, time-resolved chemical monitoring.

Here, we combine operando synchrotron SAXS/WAXS with simultaneous pH monitoring under controlled hydrodynamic conditions to resolve the coupled structural and chemical evolution of calcium carbonate precipitation. By exploiting the Porod invariant together with time-resolved pH measurements, we establish a model-independent link between structural evolution and solution chemistry without relying on assumptions about particle morphology or size distribution. This approach resolves four distinct stages of precipitation and crystallization, providing a quantitative framework for interrogating rapid mineral formation under non-equilibrium conditions.

II. RESULTS

A. SAXS and pH analysis

We first report experiments carried out at a precursor concentration of 9 mM ($CaCl_2$ and Na_2CO_3) under a stirring rate of 250 rpm, corresponding to a highly supersaturated regime, with behavior consistent across all conditions investigated. Upon mixing, the ionic activity product $IAP = \mathrm{a}(Ca^{2+})\mathrm{a}({CO_3}^{2-})$ largely exceeds the solubility product of amorphous calcium carbonate (ACC), $K_{\mathrm{sp}}^{\mathrm{ACC}} \sim 10^{-6}$, leading to a supersaturation ratio $S = \frac{\mathrm{IAP}}{K_{\mathrm{sp}}^{\mathrm{ACC}}} \gg 1$. Even when accounting for carbonate speciation at $pH \sim 10.5$, this yields S on the order of $10^2 \sim 10^3$, placing the system deep in a high-supersaturation regime.

Time-resolved SAXS measurements (Fig. 1a) reveal the emergence and evolution of nanoscale structure during calcium carbonate precipitation. Prior to mixing, the $CaCl_2$ solution shows no detectable scattering over $5s$, remaining indistinguishable from pure water and confirming the absence of pre-existing nanostructures. The time origin ($t = 0s$) is defined as the onset of mixing with the carbonate solution; the first SAXS pattern is acquired at 0.5 s, and subsequent measurements extend up to $600s$. All scattering patterns are corrected for the water capillary contribution. Immediately after mixing, well-defined oscillations appear in the scattering profiles, consistent with polydisperse spherical particles, indicating the rapid formation of calcium carbonate independent nanoparticles. Despite this early structuring, the scattering signal evolves only gradually over the first $\sim$ $38s$. Notably, around $t \approx 40$ s, the forward scattering $I(0)$ begins to increase, indicating the development of interparticle correlations and the onset of clustering. At t $\approx$ 48 s (blue curve in Fig. 1b), a pronounced change in the scattering pattern is observed. While this may suggest the emergence of larger structural features, the increase in intensity at low q could also arise from enhanced interparticle correlations, reflected in an increase of the structure factor S(q), rather than a true growth in particle size. In the Kratky representation (Fig. 1b), the principal maximum shifts from $q \approx 1.2 \times 10^{-2}$ nm^{-1} at t=1 s to $\approx 4.5 \times 10^{-3} nm^{-1}$ at t $>$ 52 s, corresponding to an increase in characteristic size from $R \sim 180nm$ to beyond $R \sim 400nm$ (see the dashed lines). Quantitative analysis reveals an initial bimodal size distribution (167 ± 13 nm and 128 ± 26 nm at t=2s), which subsequently evolves into a highly polydisperse population. Following a rapid growth burst, the main contribution to the scattering comes from particles reaching ($R = 445 \pm 80$ nm at t=67.5s, leading to strong attenuation of interference fringes. Further details on the way quantitative analysis is carried out are provided in Supplementary Section S1. By coupling pH measurements with SAXS through the Porod invariant, we directly evidence the interplay between solution chemistry and nanoscale structural transformation in real time. The general expression for the Porod invariant is

$$\boxed{\mathcal{Q}_p = 2\pi^2 r_e^2 \left\langle \left(\rho(\mathbf{r}) - \langle\rho\rangle\right)^2 \right\rangle} \tag{1}$$

which shows that the Porod invariant is directly proportional to the mean-square fluctuations of the electron

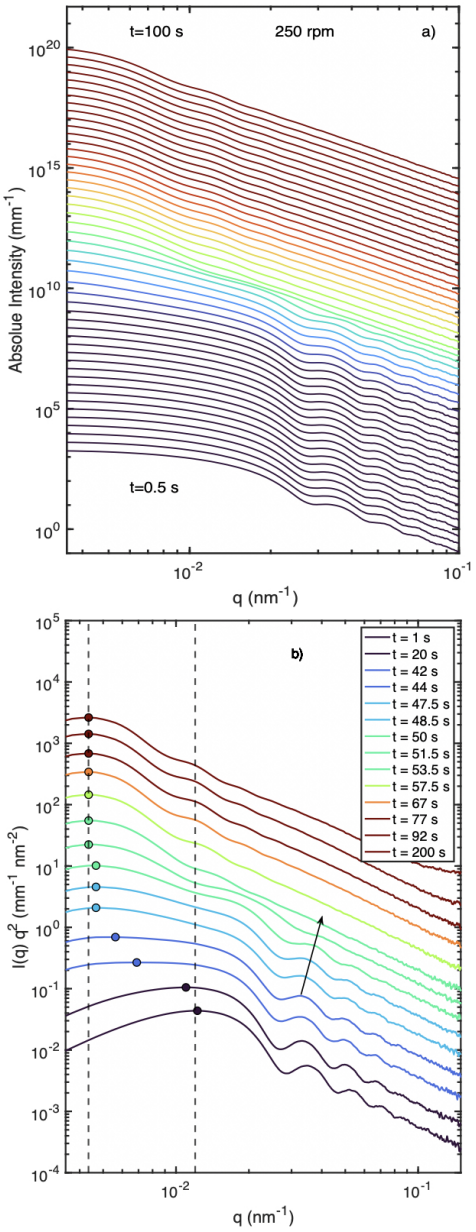


Figure 1. Time evolution of scattering curves (curves are vertically offset for clarity). a): intensity as a function of q; b): Kratky representation highlighting a subset of curves exhibiting the most pronounced changes. Colors are consistent with those used later for the pH, Porod invariant, and WAXS evolution, reflecting the key structural and chemical transformations associated with the evolution of the SAXS profiles. The arrow in Fig. 1b indicates a shift toward higher q of the first fringe, corresponding to a slight decrease in particle size between $t = 48.5\,\mathrm{s}$ and $t = 53.5\,\mathrm{s}$. The dashed lines mark the positions of the Kratky maxima at the beginning and end of the process, while the disks indicate the position of the maximum of the Kratky peak as a function of time.

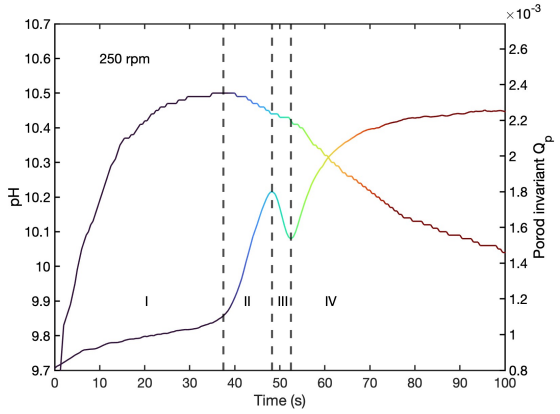


Figure 2. Simultaneous representation of pH and the Porod invariant Q_P as functions of time. The rainbow color scale highlights the key evolution of these parameters, providing essential insight into the different stages of the precipitation process. This code of color will be used alongside this study. The dashed lines delineates the boundaries of the four stages I, II, III and IV

density within the sample.

For a two-phase system consisting of particles with electron density ρ dispersed in a solvent of electron density ρ_s, the Porod invariant simplifies to

$$\boxed{\mathcal{Q}_p = 2\pi^2 (r_e \Delta\rho)^2 \phi(1-\phi)} \qquad (2)$$

where $\Delta\rho = \rho - \rho_s$ is the electron-density contrast and ϕ is the particle volume fraction. This expression provides a model-independent measure of the total scattering contrast in the system and relates the invariant directly to the volume fractions of the two phases [20, 25, 26]. Here, $r_e = 2.818 \times 10^{-6}\,\mathrm{nm}$ denotes the classical electron radius. The temporal evolution of Q_P , together with the pH (Fig. 2a), delineates four distinct stages of the precipitation pathway and directly reveals the coupling between structural development and solution chemistry. The derivatives of these quantities are shown in supplementary information S2. To our knowledge, such a time-resolved correlation between SAXS invariants and pH has not been previously reported.

We now turn to a stage-by-stage analysis of the precipitation pathway:

Stage I – Initial nucleation ($t < 38\,\mathrm{s}$). During the first $\sim 38s$, Q_P increases slightly while the pH rises sharply from ~ 7 to ~ 10.5 following carbonate addition, yet remains below the equilibrium value (pH $\approx$ 10.9). This deviation indicates rapid consumption of carbonate

ions through interaction with Ca^{2+}, consistent with the formation of nanometric calcium carbonate species. The finite values of Q_P (0.0008–0.0011) confirm the immediate presence of scattering objects, in agreement with the well-defined oscillations observed in the SAXS profiles, indicating the formation of the amorphous phase. During this period the size of the particles does not change much, while the scattered intensity at low q increases reflecting an increase in the volume fraction. At such high supersaturation ($S \sim 10^{2\smile}10^3$), the nucleation barrier becomes negligible, resulting in a burst nucleation regime. The immediate appearance of a finite Porod invariant at 0.5 s provides direct experimental evidence of this process, with Q_P acting as a real-time proxy for the rapid increase in particle volume fraction. The decrease in the rate of increase of the Porod invariant occurs over the same characteristic timescale as the evolution of the pH (see Fig. 2). Specifically, dQ_P/dt decreases by a factor of three over 30 s, while dpH/dt simultaneously drops from ~ 0.14 to nearly zero (See Supplementary information S2). Since dpH/dt reflects the rate of carbonate consumption and dQ_P/dt tracks the formation of scattering objects, this close correspondence demonstrates a direct coupling between reaction kinetics and structural evolution. The simultaneous decay of both quantities indicates that the slowdown in particle formation is governed by the rapid depletion of supersaturation, marking the end of the burst nucleation regime. The characteristic time of 38 s corresponds to the simultaneous zero-crossing of dpH/dt and the sharp increase in the Porod invariant Q_P, signaling the transition to a regime of rapid phase transformation.

Stage II – Onset of crystallization ($38 < t < 48.3\,\mathrm{s}$). In this regime, Q_P increases from 0.0011 to 0.0018 while pH decreases slightly, indicating limited net carbonate consumption. SAXS shows the progressive increase of scattering at small q ($q < 10^{-2}\mathrm{nm}^{-1}$) together with a reduction in the smallest detectable features, consistent with structural reorganization of ACC rather than classical growth of individual particles. The simultaneous increase in Q_P and I_0 at nearly constant particle radius indicates enhanced scattering, redistribution of matter within the amorphous phase with the onset of crystallization (Please refer here to Supplementary Information S3). While loose aggregation of primary particles could contribute to the increase in I_0, it cannot account for the concurrent evolution of Q_P, which instead reflects increase in the volume fraction of crystalline phase. This regime therefore corresponds to a transition from initial ACC formation to a reorganized amorphous state under continued high supersaturation and onset of crystallization.

Stage III – Amorphous destabilization and loss of structural identity ($48.3 < t < 52.5\,\mathrm{s}$). During this transient regime, pH remains nearly constant, indicating negligible net carbonate consumption. In contrast, Q_P decreases from 0.0018 to 0.0015, while SAXS reveals a bimodal size distribution dominated by an increase of the structure factor S(q) (see S.I. 3). The disappearance of form-factor oscillations indicates a loss of well-defined particle identity. It is accompanied by a sudden collapse of the structure factor at t = 52 s. This behavior is consistent with a dissolution–reorganization process in which partial breakdown of ACC leads to redistribution of material and reduction in scattering contrast. Stage III thus represents a transient loss of structural coherence that coincide with crystallization, rather than a direct topotactic solid-state transformation.

Stage IV – Complete crystallization ($t > 52.5\,\mathrm{s}$). Following this destabilization, Q_P, I_0, and particle volume increase with identical kinetics before saturating, while pH decreases strongly. This coupling demonstrates that crystalline growth is sustained by continuous consumption of dissolved carbonate species rather than by redistribution at fixed mass. The concurrent increase in scattering intensity, Porod invariant, and particle size is consistent with the formation and growth of crystalline domains from a reconfigured amorphous precursor population. WAXS confirms the emergence of vaterite and calcite, establishing that crystallization proceeds through nucleation and growth from a chemically evolving solution–particle system under progressive supersaturation depletion. The eventual saturation of all observables marks exhaustion of reactive species and approach to equilibrium.

B. WAXS analysis

To elucidate the origin of these transient features, WAXS measurements provide complementary insight (see Fig. 3). In early stages I (t < 38 s), the absence of Bragg peaks confirms the amorphous nature of the particles detected by SAXS (see Fig. 3a). In the middle of the transient regime (stage II), the pH departs from its quasi-plateau and exhibits a marked decrease (green region in Fig. 2a), providing a clear chemical signature of a change in reaction pathway.

Interestingly, this drop coincides with the abrupt emergence of crystalline reflections from vaterite and calcite (Fig. 3b), together with a pronounced non-monotonic evolution of the Porod invariant Q_P, characterized by an initial increase, a sharp minimum, and a subsequent recovery. The synchronous evolution of pH,

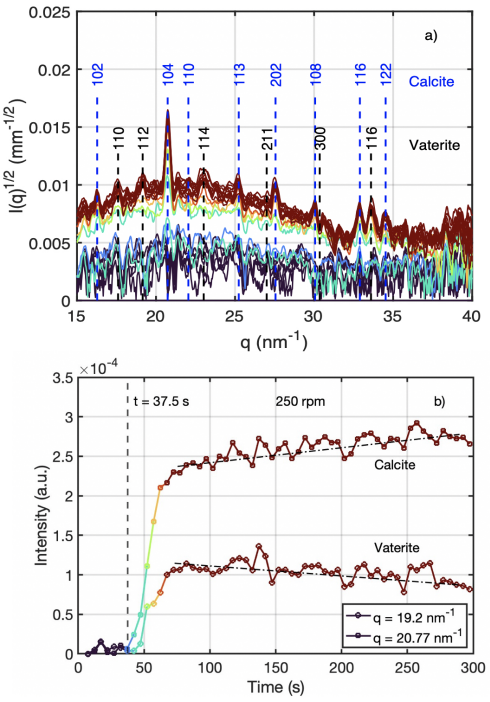


Figure 3. a) WAXS diffraction patterns integrated over 10 consecutive frames to resolve the crystalline phases of vaterite and calcite. The vaterite reflections, indexed according to the hexagonal structure [27], are indicated by black dashed lines with their corresponding Miller indices, while calcite reflections [28] are marked by blue dashed lines. The coexistence of both polymorphs is evident, with calcite peaks progressively dominating over those of vaterite. The square root of the intensity is plotted to enhance the visibility of peak evolution. The onset of crystallinity is clearly observed around t = 50s (transition between the light blue curve to the green one) for which Bragg peaks are clearly visible. b) this panel shows the temporal evolution of the Bragg peak intensities for the (112) vaterite and (104) calcite reflections. It should be noted that each WAXS pattern represents an average over 10 frames, corresponding for example at t = 50 s, to a time window from 47.5 s to 52.5 s.

Q_P, and WAXS signals demonstrates that crystallization is both structurally and chemically driven. In this context, the delayed decrease in pH, which does not occur before $t = 38$ s, together with the growth of Q_P, provides a sensitive kinetic marker for the onset of crystallization from the amorphous precursor. The concomitant emergence of calcite and vaterite indicates kinetic pathway competition, challenging a strict interpretation of Ostwald's rule of stages [29].

At longer times (stage IV t > 60 s), the relative intensities of the crystalline peaks evolve, with vaterite decreasing and calcite increasing, consistent with a dissolution–reprecipitation mechanism. These observations reveal a two-step transformation pathway: rapid crystallization of amorphous precursors into crystalline phases (vaterite and calcite), followed by a slower conversion of vaterite into the thermodynamically stable calcite phase (See Figure 3b). These processes occur on distinct timescales. The initial appearance of crystallinity takes place within seconds and reflects local atomic rearrangements within or in the immediate vicinity of pre-formed amorphous nanoparticles under high supersaturation. In contrast, the subsequent vaterite-to-calcite transformation proceeds over longer timescales and involves long-range ionic transport. This separation highlights the coexistence of a fast, locally controlled crystallization step and a slower, transport limited phase transformation. The non-monotonic evolution of Q_P, together with the WAXS signatures, thus provides direct experimental evidence for this transition. More broadly, these results demonstrate that calcium carbonate precipitation proceeds through a cascade of kinetically distinct steps, with the transient variation in Q_P emerging as a sensitive, model-free marker of the onset of crystallization. The combined evolution of the Porod invariant with the pH, the Porod plot of the data and the WAXS analysis are presented in the S4 supplementary information.

C. Influence of the stirring rate

Varying the stirring rate primarily modulates aggregation kinetics without altering the underlying transformation pathway. Increasing the stirring rate to 1000 rpm results in a systematic reduction in the characteristic particle size (from 169 ± 12, nm at 250 rpm to 106 ± 35, nm, Fig. 4a and Supplementary Information S2), accompanied by a progressive shortening of Phase II, from 37.5 s to 35 s and 31 s at 250, 500, and 1000 rpm, respectively (Figs. 4b,c). These trends indicate that hydrodynamic forcing accelerates the kinetics of particle formation while preserving the same sequence of mechanistic stages. This acceleration is attributed to enhanced collision frequencies under increased shear, which promotes faster aggregation. Concurrently, stronger hydrodynamic stresses inhibit the growth of larger aggregates, biasing the system toward smaller transient assemblies. Despite these early-time differences, all conditions converge toward similar final particle sizes (~ 420, nm, Fig. 4a), consistent with extensive coalescence and ripening that ultimately erase the initial size differences. The high polydispersity at later stages suppresses interference features, preventing detailed form-factor analysis in this regime. Overall,

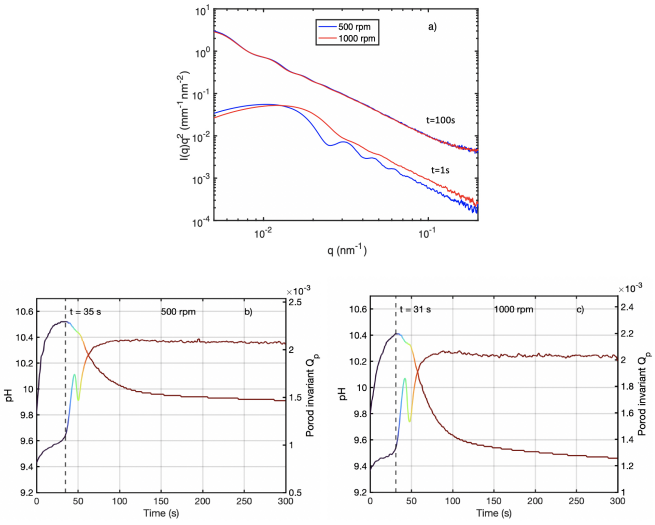


Figure 4. a) Kratky representation of the scattering intensity at t = 1 s for samples stirred at 500 rpm (blue) and 1000 rpm (red). The shift of oscillations to higher q and their stronger damping at 1000 rpm indicate the formation of smaller, more polydisperse nanoparticles. At t = 100 s, the two profiles overlap, demonstrating convergence to a common final state. (b,c) Temporal evolution of the Porod invariant Q_P and pH at 500 (b) and 1000 rpm (c). Despite marked differences in initial particle size, the precipitation pathway is invariant, evidencing a self-similar kinetic evolution across hydrodynamic conditions.

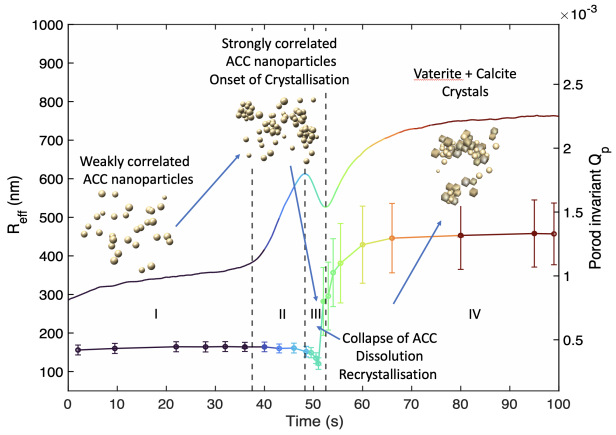


Figure 5. Time-resolved evolution of calcium carbonate precipitation for a representative stirring condition (250 rpm), illustrating the four stages identified from the Porod invariant together with the evolution of the ACC particle radius. Crystallization begins with a sharp increase in the Porod invariant accompanied by a decrease in pH (Fig. 2), following a transient reduction in particle radius associated with the dehydration of amorphous calcium carbonate (ACC) nanoparticles. The fast disappearance of the ACC phase is marked by a sharp decrease in the Porod invariant and a further reduction in the ACC particle radius. This is followed by a renewed increase in the Porod invariant, coincident with the growth of large crystalline particles.

these observations support a scenario in which hydrodynamic conditions tune kinetic rates accelerating aggregation and limiting transient growth without modifying the intrinsic non-classical aggregation driven mechanism governing particle formation (See S4 as well).

III. DISCUSSION

The formation of crystalline calcium carbonate from aqueous solution is commonly described either within classical nucleation theory (CNT) [30, 31] or via non-classical pathways involving pre-nucleation clusters, dense liquid intermediates, and amorphous precursor phases [3–5, 22]. Under the extreme supersaturation conditions investigated here, particle formation occurs on timescales too rapid to resolve any intermediate species. Instead, amorphous calcium carbonate (ACC) nanoparticles form quasi-instantaneously with a characteristic radius of $R \sim 160$ nm. The experimentally accessible pathway therefore corresponds to the subsequent evolution of this dense amorphous dispersion toward crystallization. The coupling between the experimental observables is summarized in Fig. 5, where panel (a) reports the time evolution of pH and the Porod invariant, while panel (b) shows the corresponding evolution of the particle radius. This combined representation shows direct correlation between chemical driving forces and structural response throughout the reaction.

Operando SAXS-WAXS combined with pH monitoring reveals that the transformation proceeds through four distinct stages during which density fluctuations and crystallization remain strongly coupled. Immediately after mixing, the system consists of a dense but weakly correlated ACC dispersion characterized by nearly constant particle size, only minor variations of the Porod invariant, and $S(0) \approx 1.08$ (Supplementary Fig. S3). The SAXS profiles display a low-q upturn together with a shallow minimum in $S(q)$, consistent with the progressive amplification of long-wavelength density correlations, while no crystalline Bragg reflections are yet detected by WAXS. Importantly, the absence of a well-defined finite-q maximum rules out classical spinodal decomposition and instead indicates a fluctuation-dominated metastable regime characterized by increasing compressibility and continuously evolving correlation lengths.

During stages II and III, the system enters a fluctuation-amplified regime in which crystallization develops within the correlated ACC network itself most likely at the surface of ACC nanoparticles as demonstrated in previous studies [32]. The forward scattering intensity increases dramatically, with $S(0)$ rising by more than one order of magnitude while the ACC particle radius remains nearly constant or decreases slightly. The increase in low-q scattering therefore does not originate from ACC particle growth, but from amplification of collective density correlations related to the emergence of crystalline particles. The slight reduction in ACC particle size can be interpreted as dehydration, as commonly reported in the literature [6].

Simultaneously, weak calcite and vaterite Bragg reflections emerge and progressively increase in intensity while the ACC SAXS contribution remains dominant. Crystalline order is therefore already established before disappearance of the amorphous scaffold, indicating that nucleation occurs in contact with a dynamically correlated ACC matrix rather than through the independent appearance of a separate crystalline population. This interpretation is reinforced by the coupled evolution of the Porod invariant, $S(0)$, and the ACC effective radius. During phase II, the Porod invariant increases markedly while both pH and Ca^{2+} activity decrease slightly, indicating the progressive development of crystalline order together with limited but measurable ion consumption from solution. Simultaneously, the Kratky maximum shifts progressively toward lower q, revealing the emergence of increasingly long-range mesoscale correlations within the fluctuation-amplified ACC network.

A critical transition then occurs in phase III. The ACC form-factor oscillations progressively disappear, the effective ACC radius decreases, and $S(0)$ collapses sharply while calcite Bragg intensities continue to increase. Simultaneously, the Porod invariant and Q_P decrease markedly, demonstrating a progressive loss of ACC scattering mass and structural coherence.

Together, these observations indicate that the crystalline phase grows at the expense of the ACC phase, which is continuously consumed during the transformation. In this regime, ACC does not persist as a stable coexisting population but is progressively depleted as crystalline domains develop and expand throughout the system.

Importantly, this transformation occurs with no measurable net change in Ca^{2+} or CO_3^{2-} activity, indicating that crystal growth proceeds without significant exchange with the bulk solution (see Supplementray Information S5). This behavior is consistent with a tightly coupled transformation in which ACC is converted into crystalline material (calcite + vaterite) through concomitant dissolution and reprecipitation at the nanoscale. Although the transient appearance of ACC is broadly consistent with Ostwald's rule of stages, the concomitant nucleation of calcite and vaterite points to kinetic pathway competition rather than a strictly sequential progression through metastable phases.

Our combined SAXS–WAXS results support a mechanism in which crystalline domains progressively emerge within the metastable ACC network, grow at its expense, and ultimately replace it as the dominant structural component. The disappearance of the ACC SAXS contribution therefore reflects both the loss of amorphous structural coherence and the collapse of the hydrated fluctuation network that initially stabilizes the amorphous phase.

Notably, the ACC to crystal transformation is extremely rapid, occurring on a timescale of only a few seconds. This rapid evolution is accompanied by a concerted decrease in the Porod invariant and ACC form-factor contribution, together with a simultaneous increase in calcite Bragg intensities, indicating that the loss of ACC scattering mass is directly coupled to the growth of crystalline order.

Our observations are consistent with previous reports of ACC transformation into crystalline phases based on TEM (e.g. Nielsen *et al.* [32]), but extend these findings to a fully quantitative, operando description over a vastly larger ensemble of particles. In particular, all scattering observables—including the model-free Porod invariant—coherently track the transformation across length scales and time, providing a unified view of the coupled amorphous-to-crystalline conversion.

Taken together, these observations indicate that crystallization proceeds through a dynamically coupled fluctuation–ordering pathway in which the crystalline phase develops coherently in contact with the metastable ACC network and progressively consumes it during growth.

CONCLUSION

In summary, operando SAXS–WAXS combined with pH monitoring reveals a fully time-resolved pathway for calcium carbonate formation under extreme supersaturation. Rather than proceeding through direct crystal nucleation or through a sequence of structurally preserved intermediates, the system evolves through a coupled fluctuation–crystallization process in which a dense amorphous nanoparticle dispersion undergoes hierarchical restructuring, strong amplification of long-

wavelength density correlations, and progressive emergence of crystalline order.

A key mechanistic feature is the transient coexistence of amplified amorphous fluctuations with growing crystalline Bragg reflections, demonstrating that crystallization initiates within a correlated amorphous environment rather than after disappearance of the precursor phase. The subsequent loss of ACC form-factor coherence together with the collapse of the low-q scattering signal indicates that continued crystalline growth destabilizes the metastable amorphous network, ultimately leading to loss of its structural persistence. These findings suggest that neither classical nucleation,interpreted as direct crystallization from solution [30, 31] nor a strict interpretation of the Ostwald rule of stages [29, 33, 34] fully captures the crystallization dynamics observed under extreme supersaturation. Rather than a sequence of discrete phase transformations, the data reveal a far-from-equilibrium pathway in which a correlated amorphous precursor destabilizes into competing crystallization channels, governed by coupled structural density fluctuations and mesoscale correlations. The concomitant nucleation of calcite and vaterite from the amorphous precursor highlights parallel crystallization pathways, inconsistent with a strictly sequential Ostwald progression. Their subsequent evolution is controlled by differences in growth kinetics and thermodynamic stability, resulting in the eventual predominance of calcite.

More broadly, this work establishes an experimental framework for investigating crystallization under strongly non-equilibrium conditions, where phase selection is governed not only by nucleation barriers but also by the collective dynamics, stability, and restructuring of transient amorphous states. The results highlight fluctuation-amplified precursor networks as central actors in multistage mineralization pathways and demonstrate that crystallization can emerge through cooperative restructuring of correlated amorphous matter rather than through independent nucleation and growth events.

IV. MATERIALS AND METHODS

Calcium chloride dihydrate $CaCl_2, {}_2H_2O$, sodium carbonate monohydrate $Na_2CO_3 \cdot H_2O$ were used as received from Aldrich. Precursor solutions were prepared in Milli-Q water (18.2 $M\Omega cm$) at a concentration of 9 mM. In situ SAXS experiments were conducted at the European Synchrotron Radiation Facility (ESRF, Grenoble, France) on the ID02 beamline. The incident energy was 12.23 keV ($\lambda = 0.101nm$), and a sample-to-detector distance of 15 m provided a q-range of 0.003–0.5 nm^{-1}. The beam size at the sample was $150\mu m \times 150\mu m$. All measurements were performed using a flow-through setup, with the flow rate set to the maximum attainable value of 370 μls^{-1} (See Supplementary Information S6 for the set-up). Prior to each experiment, 50 ml of a $CaCl_2 \cdot 2\,H_2O$ solution was inserted in a beaker equipped with a digitally controlled stirrer operating between 250 and 1000 rpm. The dimensions of the beaker (diameter = 6 cm and height = 8 cm) and the stirrer (length = 2.5 cm) were kept constant throughout the experiments to prevent any unwanted effects from these parameters. After preparation of the $CaCl_2 \cdot 2\,H_2O$ solution, the inlet and outlet tubing of the flow system were immersed in the beaker. A computer-controlled Vevor dispensing system was used to inject 50 ml of a $Na_2CO_3 \cdot H_2O$ solution into the beaker within 2 s. Note that the injection method plays a crucial role. In this case, a tube connected to the Vevor system was immersed to the bottom of the beaker, ensuring that mixing occurred near the stirrer. This setup also helped reduce the formation of air bubbles during injection. The same procedure was consistently followed throughout all experiments. Data acquisition started 5 s prior to the sodium carbonate injection and continued for 400 s thereafter in order to capture the precipitation kinetics. The typical exposure time was 0.1 s per frame, with frames collected at 0.5 s intervals. After each experiment, the tubing was cleaned by flushing with 0.1 M citric acid, followed by rinsing with distilled water. Throughout the experiments, the pH was continuously monitored using a Mettler Toledo pH meter, allowing the pH evolution to be correlated with each recorded scattering frame. All experiments were carried out at room temperature $T = 25\,^{\circ}C$. Two-dimensional SAXS patterns were recorded using an Eiger2 4M detector and normalized to absolute intensity. Azimuthal averaging yielded one-dimensional profiles, and water background scattering was subtracted. Simultaneous WAXS measurements were performed with a Rayonix LX170-HS CCD detector (sample-to-detector distance 0.126 m), covering a q-range of 5.9 to 44.3 nm^{-1}. Continuous pH monitoring (Mettler Toledo) enabled frame-by-frame correlation between structural and chemical evolution.

AUTHORS CONTRIBUTION

AG, YC, SA, BC, OG, SU, RSP carried out the experiments. AG, BC, SU designed the project, AG, YC analyzed the data. SU and OG carried out experiments on Ca2+ activity and turbidity in Turkye. All authors discussed the content of the paper and AG wrote the

article.

ACKNOWLEDGEMENTS

The authors are especially grateful to the ESRF for beamtime at the beamline ID02 (proposal MA-6908) and Theyencheri Narayanan and Jean Daillant for the discussions. We also acknowledge the Partnership for Soft Condensed Matter (PSCM) at the ESRF for providing the necessary chemicals and the support laboratories during our beamtime. BC would like to thank the Norwegian Research Council for financial funding through ICONIC (FRINATEK, Project No. 303252). SU and OG acknowledge the support from the Scientific and Technological Council of Turkiye (TUBITAK) under project 121C137.

Conflict of interest The authors declare no conflict of interest nor competing financial interests.

Supplementary information is provided

* Corresponding authors: alain.gibaud@univ-lemans.fr, yuriy.chushkin@esrf.fr

[1] J. J. D. Yoreo, P. U. P. A. Gilbert, N. A. J. M. Sommerdijk, R. L. Penn, S. Whitelam, D. Joester, H. Zhang, J. D. Rimer, A. Navrotsky, J. F. Banfield, A. F. Wallace, F. M. Michel, F. C. Meldrum, H. Cölfen, and P. M. Dove, Science **349**, aaa6760 (2015).

[2] A. Putnis, Rev. Mineral. Geochem. **70**, 299 (2009).

[3] E. M. Pouget, P. H. H. Bomans, J. A. C. M. Goos, P. M. Frederik, G. de With, and N. A. J. M. Sommerdijk, Science **323**, 1455 (2009).

[4] D.Gebauer, J. Gale, and H.Cölfen, Science **322**, 1819 (2008).

[5] D. Gebauer, M. Kellermeier, J. Gale, L. Bergström, and H. Cölfen, Small **18**, 2107735 (2022).

[6] J. Ihli, W. C. V. Wong, E. Noel, Y.-Y. Kim, A. Kulak, H. Christenson, M. Duer, and F. Meldrum, Nature communications **5**, 3169 (2014).

[7] M. B. Short, J. C. Baygents, J. W. Beck, D. A. Stone, R. S. Toomey, and R. E. Goldstein, Phys. Rev. Lett. **94**, 018501 (2005).

[8] V. Schoeppler, R. Lemanis, E. Reich, T. Pusztai, L. Gránásy, and I. Zlotnikov, Proceedings of the National Academy of Sciences **116**, 20388 (2019), https://www.pnas.org/doi/pdf/10.1073/pnas.1907229116.

[9] A. V. Radha, T. Z. Forbes, C. E. Killian, P. U. P. A. Gilbert, and A. Navrotsky, Proceedings of the National Academy of Sciences **107**, 16438 (2010), https://www.pnas.org/doi/pdf/10.1073/pnas.1009959107.

[10] S. Muryanto, A. Bayusenob, H. Ma'munb, and Jotho, Procedia Chemistry , 69–76 (2014).

[11] J. Rodriguez-Blanco, S. Shaw, and L. Benning, Nanoscale **3**, 265 (2011).

[12] O. Cherkas, T. Beuvier, F. Zontone, Y. Chushkin, L. Demoulin, A. Rousseau, and A. Gibaud, Advanced Powder Technology **29**, 2872 (2018).

[13] L. Kuhrts, H. Shaked, J. Sklar, E. Prudnikov, S. Prévost, G. Manna, M. Sztucki, A. Katsman, and B. Pokroy, Proceedings of the National Academy of Sciences **122**, e2421961122 (2025).

[14] R. Berner, J. Westrish, R. Graber, J. Smith, and C. S. Martens, American Journal of Science **278**, 816 (1978).

[15] Y. Pan, Y. Li, Q. Ma, H. He, S. Wang, Z. Sun, W.-J. Cai, B. Dong, Y. Di, W. Fu, and C.-T. A. Chen, Marine Chemistry **237**, 104036 (2021).

[16] G. M. Marion, F. J. Millero, and R. Feistel, Ocean Science **5**, 285 (2009).

[17] P. J. M. Smeets, K. Cho, R. Kempen, N. Sommerdijk, and J. D. Yoreo, Nature Materials **14**, 394–399 (2015).

[18] T. Beuvier, E. Chavez, P. Kwasniewski, S. Marre, C. Lecoutre, Y. Garrabos, C. Aymonier, B. Calvignac, and A. Gibaud, LabonaChip **15** (2015), 10.1039/C5LC00115C.

[19] J. Bolze, B. Peng, N. Dingenouts, P. Panine, T., and M. Ballauff, Langmuir **18**, 8364–8369 (2002).

[20] A. Gibaud, D. Younas, L. Matthews, T. Narayanan, K. Longkaew, I. U. Hageberg, Y. Chushkin, D. W. Breiby, and B. Chattopadhyay, Journal of Applied Crystallography **56**, 1114 (2023).

[21] H. Du, M. Steinacher, C. Borca, T. Huthwelker, A. Murello, F. Stellacci, and E. Amstad, Journal of the American Chemical Society **140**, 14289 (2018).

[22] D. Gebauer, M. Kellermeier, J. Gale, L. Bergström, and H. Cölfen, Chem. Soc. Rev. **43**, 2348 (2014).

[23] Q. Zhao, P. Duchstein, B. Demmert, T. Q. N. Dao, K. Anjala, E. Gruber, F. Gröhn, D. Zahn, D. E. Jacob, and S. E. Wolf, Advanced Functional Materials **n/a**, e29192 (2026).

[24] T. Narayanan, M. Sztucki, T. Zinn, J. Kieffer, A. Homs-Puron, J. Gorini, P. Van Vaerenbergh, and P. Boesecke, J. Appl. Crystallogr. **55**, 98 (2022).

[25] G. Porod, *General theory*, edited by O. Glatter and O. Kratky, Vol. 15 (Academic Press., 1982) pp. 17–51.

[26] J. Liu, S. Pancera, V. Boyko, A. Shukla, T. Narayanan, and K. Huber, Langmuir **26**, 17405 (2010).

[27] S. R. Kamhi, Acta Crystallographica **16**, 770 (1963).

[28] H. Effenberger, K. Mereiter, and J. Zemann, Zeitschrift für Kristallographie - Crystalline Materials **156**, 233 (1981).

[29] W. Ostwald, Z. Phys. Chem. **22**, 289–330 (1897).

[30] M. Volmer and A. Weber, Zeitschrift für Physikalische Chemie **119**, 277 (1926).

[31] K. Kelton and A. Greer, in *Nucleation in Condensed Matter*, Pergamon Materials Series, Vol. 15, edited by K. Kelton and A. Greer (Pergamon, 2010) pp. 19–54.

[32] M. H. Nielsen, S. Aloni, and J. DeYoreo, Science **345** (2014), 10.1126/science.1254051.

[33] J. J. D. Yoreo, Proceedings of the National Academy of Sciences **119**, e2121661119 (2022), https://www.pnas.org/doi/pdf/10.1073/pnas.2121661119.

[34] P. T. Cardew, Crystal Growth & Design **23**, 3958 (2023).

Supplementary Files

This is a list of supplementary files associated with this preprint. Click to download.

- CaCO3SIfinal.pdf